

# Urbanization impacts on Pearl River Delta extreme rainfall - sensitivity to land cover change vs anthropogenic heat

Chenxi Hu<sup>1</sup>, Kwun Yip Fung<sup>2</sup>, Chi-Yung Francis Tam<sup>3</sup>, and Ziqian Wang<sup>4</sup>

<sup>1</sup>the Chinese university of Hong Kong

<sup>2</sup>University of Texas at Austin

<sup>3</sup>Chinese University of Hong Kong

<sup>4</sup>Sun Yat-sen University

November 23, 2022

## Abstract

Impacts of urban land cover and anthropogenic heat (AH) on extreme local rainfall over the coastal PRD megacity region during boreal summer are investigated by conducting numerical experiments using the Weather Research and Forecasting (WRF) model coupled with a single-layer urban canopy model (SLUCM). To examine the relative importance of land cover change vs the presence of AH, three numerical experiments corresponding to different levels of urbanization in the PRD area were designed: one with cropland covering the whole region, one with urban land cover but zero AH, and one with urban land cover and a strong diurnal maximum of  $300\text{Wm}^{-2}$  of AH in the model simulations. Results show that the increase of accumulated rainfall in the urban area is much more sensitive to the intensity of AH than the mere change of surface properties. Urbanization with intense AH can enhance both the intensity and frequency of extreme rainfall, which can be attributed to higher surface temperature (of about  $3.5$  to  $4^\circ\text{C}$ ), higher convective available potential energy (CAPE), and lower convective inhibition (CIN), thus creating an environment more conducive to strong convection over the urban areas. Moreover, enhanced rainfall is supported by moisture supply from the South China Sea and increased water vapor flux convergence over the PRD city area. The amount of moisture flux converging over the coastal megacity area was found to depend on the direction of prevailing background wind.

# **Urbanization impacts on Pearl River Delta extreme rainfall – sensitivity to land cover change vs anthropogenic heat**

Hu Chenxi<sup>1</sup>, Kwun Yip Fung<sup>1,2</sup>, Chi-Yung Tam<sup>1</sup> and Wang Ziqian<sup>3,4</sup>

<sup>1</sup>Earth System Science Programme, the Chinese University of Hong Kong, Hong

Kong, China

<sup>2</sup>Geological Sciences, Jackson School of Geoscience, The University of Texas at

Austin, Austin, TX, USA

<sup>3</sup>School of Atmospheric Sciences, and Key Laboratory of Tropical Atmosphere-

Ocean System (Ministry of Education), Sun Yat-sen University, Zhuhai, China

<sup>4</sup>Southern Marine Science and Engineering Guangdong Laboratory (Zhuhai), Zhuhai,

China

Submitted to Earth and Space Science

November 2020

ORCID: 0000-0002-8397-9319 (Hu Chenxi), 0000-0003-1213-165X (Kwun Yip Fung),

0000-0002-5462-6880 (Chi-Yung Tam), 0000-0001-8113-9941 (Wang Ziqian).

Key points:

- Extreme rainfall is sensitive to the extent of urbanization in the Pearl River Delta area, in which anthropogenic heat play a crucial role
- Higher CAPE, lower CIN, and more moisture flux convergence due to urban heat island effect can lead to stronger extreme rainfall

- Though urbanization reduces surface evaporation, moisture supply from the ocean can still support the intensification of extreme rainfall

Keywords: Coastal megacities, urban heat island effect, anthropogenic heat, extreme rainfall, WRF model simulations

---

Corresponding author address: Dr. Chi-yung Francis Tam, Earth System Science Programme, the Chinese University of Hong Kong, Hong. Email: [Francis.Tam@cuhk.edu.hk](mailto:Francis.Tam@cuhk.edu.hk)

## **Abstract**

Impacts of urban land cover and anthropogenic heat (AH) on extreme local rainfall over the coastal PRD megacity region during boreal summer are investigated by conducting numerical experiments using the Weather Research and Forecasting (WRF) model coupled with a single-layer urban canopy model (SLUCM). To examine the relative importance of land cover change vs the presence of AH, three numerical experiments corresponding to different levels of urbanization in the PRD area were designed: one with cropland covering the whole region, one with urban land cover but zero AH, and one with urban land cover and a strong diurnal maximum of  $300\text{Wm}^{-2}$  of AH in the model simulations. Results show that the increase of rainfall in the urban area is much more sensitive to the intensity of AH than the mere change of surface properties. Urbanization with intense AH can enhance both the intensity and frequency of extreme rainfall, which can be attributed to higher surface temperature (of about  $3.5$  to  $4^{\circ}\text{C}$ ), higher convective available potential energy (CAPE), and lower convective inhibition (CIN), thus creating an environment more conducive to strong convection over the urban areas. Moreover, enhanced rainfall is supported by moisture supply from the South China Sea and increased water vapor flux convergence over the PRD city area. The amount of moisture flux converging over the coastal megacity area was found to depend on the direction of prevailing background wind.

## 1. Introduction

The effects of urbanization on the local climate such as extreme precipitation has become a hot research topic since last century, with rapid urbanization be observed over the globe scale (Hannah, 2018). It is reported that the urban influence on precipitation tends to be found in downwind area of urban (Changnon 1968, Huff and Changnon, 1986). After these pioneering works, many researches also reported urban impacts on precipitation, especially over locations downwind of cities. Shepherd and Burian found that the strongest annual mean precipitation is located in the downwind of Houston by analyzing Tropical Rainfall Measuring Mission (TRMM) data from January 1998 to May 2002 (Shepherd and Burian, 2003). Besides, by numerical simulating two extreme precipitation cases in Atlanta, Shem and Shepherd (2009) showed that the center of rainfall increment caused by the urban heat island (UHI) effect was located downwind of the city, by 10 to 13%.

However, the influence of urbanization is complex and might depend on the intensity of UHI and geographical locations. Studies focused on Beijing found that strong UHI effect can increase rainfall directly over the downtown area of Beijing, while for weak UHI, rainfall would be bifurcated and avoid the city center (Dou et al., 2015, and Zhang et al., 2017). For coastal locations, there are stronger and more frequent extreme rainfall over coastal urban area such as Osaka Kinki and the Tokyo metropolitan region, which can be attributed to stronger sensible heat flux, lower atmospheric stability, stronger vertical convection, and more water vapor supply from the ocean (Kusaka, 2014; Shimadera et al., 2015; Xiao et al., 2020). A summary of results on urban influence on rainfall was recently given by Lin and Niyogi (2019). The increase in precipitation intensity induced by urbanization can reach about 11% (14%) to 21% (22%) over the urban (downstream) area, but weak over other regions.

China has experienced rapid urbanization during recent few decades, and the PRD megacity is one of the urban clusters with fast urbanization. Based on station data and satellite reanalysis data, it was found that there are stronger and more frequent extreme rainfall induced by urban expansion over PRD in recent years; stronger afternoon rainfall can be observed in urban locations in the region, compared to that in the surrounding rural area (Wang et al. 2015; Chen et al., 2015). PRD urban locations also tend to see faster increasing trends of extreme rainfall frequency and more extreme rainfall events, characterized by abrupt and shorter duration episodes (Wu et al. 2018; Yan et al. 2020). Besides, it was found that the extreme rainfall intensity, spatial distribution and frequency are highly sensitive to the urban surface heat flux. Based on numerical model experiments, stronger anthropogenic heat (AH) leads to stronger and more frequent extreme rainfall over the PRD urban area (Holst et al. 2016; Fung et al. 2020).

Overall, extreme urban precipitation- with related hazards such as urban flooding- is becoming more and more common in China and can cause great economic and life losses (Yang et al. 2015). However, deeper understanding of the physical mechanisms of urban impact on precipitation is required, and the relative contribution of urban land cover and AH on extreme rainfall enhancement needs to be ascertained. This study seeks to investigate (1) the sensitivity of extreme rainfall to land cover change vs anthropogenic heat, and (2) physical mechanisms of urban impacts on extreme precipitation over the coastal PRD area. This is done by dynamical downscaling cases from General Circulation Model (GCM) outputs with a high resolution weather scale model coupled with urban canopy model, under different land cover and AH intensity. A description of the model and experimental

settings are given in section 2; results from the model simulated experiments are describe in section 3; discussions and conclusions can be found in section 4.

## **2. Methodology**

### **2.1 Model configuration and case selection**

In this study, the Weather Research and Forecasting (WRF) model with the Advanced Research WRF (ARW) dynamical core version 3.8.1 was utilized to dynamically downscale general circulation model (GCM) outputs, generated by the Geophysical Fluid Dynamical Laboratory Earth System model version 2 (GFDL-ESM2M; Dunne et al. 2012, 2013)<sup>1</sup>. The atmospheric component of GFDL-ESM2M has horizontal resolution of 2°x 2.5° in latitude and longitude, and its ocean component is the Modular Ocean Model version 4 (MOM4). The model was adopted by many studies (e.g., McSweeney et al. 2015); it performs reasonably well in simulating the East Asia monsoon circulation. By comparing its simulations with TRMM-V3B42 or ERA-Interim reanalysis data during, the model gives reasonable summertime (May-to-September) rainfall distribution and 850hPa flow, albeit with slightly underestimated mean precipitation over South China (figures not shown).

For the WRF simulations, three nested domains were used for the dynamical downscaling with one-way nesting adopted. Figure 1a shows the WRF nested domains, with domain 1 (at 50km x 50km resolution), domain 2 (at 10km x 10km resolution) and domain 3 (2km x 2km resolution) covering the East Asia/western North Pacific area (2.23-43.82N, 70.81-147.05E), South China (19.94-27.09N, 110.68-117.60E) and PRD (21.5-23.83N, 112.51-115.04E), respectively. In each domain, results from the buffer zones (4 grids boxes from the boundary) were not

---

<sup>1</sup> In our companion study by Fung et al. (2020), outputs from the same GFDL-ESMSM are downscaled for assessing the relative impacts of climate change and urbanization on PRD extreme rainfall.

considered in our analyses. There were 39 vertical levels, reaching the height of  $\sim 23\text{km}$ . Physical parameterizations in WRF included the Rapid Radiative Transfer Model for General Circulation Model (RRTMG) for the longwave radiation (Iacono et al. 2008), the short wave radiation scheme by Dudhia (1989), the WRF single-moment 6-class microphysics scheme (Hong et al. 2006), the Eta Similarity similarity theory for the surface layer options (Janjic. 1994), the NOAH land-surface model (LSM), which supports the Single Layer Urban Canopy Model (SLUCM) (Kusaka et al., 2001; Chen and Dudhia, 2001; Tewari et al. 2008), the Bougeault and Lacarrere planetary boundary layer (PBL) scheme (Bougeault et al. 1989), and the simplified Arakawa-Schubert (SAS) cumulus parameterization (for the outermost domain only; Han and Pan 2011). To ensure that WRF can reproduce the same synoptic-scale circulation from the parent model, spectral nudging is applied in the outmost domain (d01) and strength of  $3 \times 10^{-4} \text{ s}$  for U, V wind above 500hPa, at the wavelength of about 1300km.

Extreme rainfall cases to be downscaled were identified based on daily rainfall from GFDL-ESM2M. In particular, daily precipitation averaged over the region of 17-27N, 105-117E from a GFDL-ESM2M run (from 1946 to 2005) was first computed. Days during which the daily mean rainfall is larger than the 99th percentile (based on rainfall in wet days, defined as days with rain rate  $> 0.1\text{mm/day}$ ) were defined as extreme rain days. About 60 cases from May to September were chosen and were dynamically downscaled by WRF in d01. Downscaling results were then inspected, and only cases giving rainfall patterns consistent with the GFDL-ESM2M outputs were considered. We further stratified cases into those related and not related to TC occurrence (referred to as TC and non-TC cases, respectively). This was achieved by inspecting their rainband organization; cases with anticlockwise



spiral rainbands were regarded as TC cases, and the rest as non-TC cases. 26 non-TC cases were dynamically downscaled over the PRD region to 2km x 2km of resolution, with each integration starting (ending) 72 hours prior to (after) the identified extreme rain day.

## 2.2 Experimental design and UCM set up

After case selection, three sets of parallel numerical experiments were carried out for examining the sensitivity of extreme rainfall to urban land use and AH over the PRD region. In experiment 1 (referred to as NO-URBAN), the PRD urban area was replaced by “cropland” in the land use categorization in the WRF simulations, since most surrounding areas of the PRD megacity are cropland. For Experiment 2 and 3 (referred to as AH0 and AH300, respectively), WRF coupled with SLUCM were utilized with different values of AH ( $0\text{W/m}^2$  and  $300\text{W/m}^2$  for diurnal maximum). 2002 land use categorization based on the Moderate Resolution Imaging Spectroradiometer (MODIS) data, consisting of 17 types of land cover, was adopted in WRF-SLUCM. Figure 1b gives the land use categories within domain 3 such as Water (blue shading in Figure 1b), Evergreen Needleleaf Forest, Evergreen Broadleaf Forest, Deciduous Needleleaf Forest, Deciduous Broadleaf Forest, Mixed Forest (green), Closed Shrublands, Open Shrublands, Woody Savannas, Savannas (pink), Grasslands (cyan), Permanent Wetlands, Croplands (yellow), Urban and Built-up (red), Natural Vegetation Mosaic, Snow and Ice (white), and Barren (black), also shown are the locations of major cities in PRD, namely, Hong Kong (HK), Shenzhen (SZ), Dongguan (DG), Guangzhou (GZ), Foshan (FS), Zhongshan (ZS), Zhuhai (ZH), and Macao (MC) (see black dots). SLUCM can incorporate three types of urban categories: “Low Intensity Residence”, “High Intensity Residence”, and “Commercial and Industrial”. Due to lack of data in MODIS, all urban grid points were categorized

as High Intensity Residence. Figure 1c shows the land use distribution of NO-URBAN experiment, with the urban land cover replaced by cropland in all domains.

Table 1 gives UCM parameters prescribed for MODIS land cover. The mean building height was set to 30m (based on data from the Hong Kong Lands Department). The standard deviation of building height was 4m, and the road width was 16m, based on default values for commercial land use. Satellite measurements indicated that a  $289\text{W m}^{-2}$  diurnal peak value in AH in Hong Kong during summer (Wong et al., 2015). For the AH300 experiments, a diurnal AH profile with maximum at midnight to about 9 am, and minimum at 8 pm local time was adopted in SLUCM (see Holst et al., 2016); AH was set to zero for the AH0 runs. The former choice thus represents a high urbanization scenario, equivalent to having commercial and industrial land use over every urban location within PRD.

### **3. Results**

#### **3.1 Surface temperature**

Figure 2a shows the AH0 minus NO-URBAN surface albedo in the innermost model domain. Compared with natural land cover in NO-URBAN, the surface albedo decreased by about 40% to 45% (see Figure S1) over the original urban area in AH0 (or in fact AH300, which gives the same albedo as AH0). Lower surface albedo over the urban area can lead to more absorbed shortwave radiation, and therefore stronger sensible heat flux compared with rural areas. Also shown in Figure 2 is the 2-m temperature difference between experiments AH0 and NO-URBAN, and also between AH300 and NO-URBAN. It is noteworthy that AH0 experiment gives higher temperature than NO-URBAN over almost the whole urban area in PRD (see Figure 2b), meaning that the presence of a megacity itself can lead to higher temperature,

even if there is no AH released within the city. The warming magnitude ranges from 0.5 to 2°C; over more inland/northern PRD urban locations, change of 2-m temperature can reach 1.5°C or more. On the other hand, warming outside the urban area is rather small ( $< 0.5^{\circ}\text{C}$ ), meaning that the influence of surface properties on the temperature is very localized. Overall, surface warming is likely caused by the decrease of surface albedo, which can lead to more shortwave radiation received over the megacity area. In addition, complex building structures can hold more heat, which can also contribute to warmer temperature within the megacity.

Figure 2c gives the 2-m temperature difference between AH300 and NO-URBAN. It can be seen that, with the presence of AH, temperature within the city area can increase by  $\sim 2$  to  $4^{\circ}\text{C}$ . More than  $3.5^{\circ}\text{C}$  warming was found in northwestern and northeastern parts of the megacity. The 2-m temperature anomaly pattern in Figure 2c is very similar to that in Figure 2b. Finally, it is noteworthy that warming due to changes in land surface only (i.e. difference between NO-URBAN and AH0) is about  $1.2^{\circ}\text{C}$  averaged over the urban area, while the presence of AH (i.e. between AH300 and AH0) can lead to about  $1.65^{\circ}\text{C}$  increase in temperature of the city. Thus, under such a high urbanization scenario, AH appears to have a stronger effect on the urban surface temperature.

In addition to changes in the surface temperature, we have also examined the vertical temperature profiles (see Figure S2). The temperature difference between NO-URBAN and the other two experiments is largest at the surface, with temperature anomaly of  $\sim 0.3^{\circ}\text{C}$  ( $0.76^{\circ}\text{C}$ ) at 200m for AH0 (AH300). Such warming due to either changes in surface properties, or increased AH, decreases with height, with the temperature difference between AH0 (AH300) and NO-URBAN. vanishing at 0.6km (1.4km). It is obvious that the warming effect due to urbanization has limited vertical

extent. On the other hand, at 800m (1600m) altitude for AH0 (AH300), temperature is actually lower than that in the NO-URBAN experiment. Cooler temperature might be the result of the enhanced cloud fraction over the urban area, which leads to radiative cooling in the atmosphere. Further analysis revealed that the cloud fraction averaged over all layers increased more than 5% over most urban locations for AH0 (over whole urban area and some downstream locations for AH300) compared with NO-URBAN (see Figure S3)

### 3.2 Precipitation

In order to investigate the impact of urbanization on the occurrence of extreme rainfall characteristics, probability density functions (PDF) of hourly precipitation rates over all urban grids for all rainfall events were considered. Figure 3a shows the rainfall PDF results for NO-URBAN, AH0, and AH300. Comparing AH300 with NO-URBAN, it is seen that the rainfall occurrence increases significantly for rain rates larger than 10mm/hr. AH0 also gives higher probability of heavy rainfall compared to NO-URBAN, but only with a small difference (no more than 20% for 10 mm/hr to 100mm/hr). However, for hourly rainfall in the range of 60-110mm/hr, the frequency increases drastically by about 2.5 to 3 times due to both urban land cover and AH. In general, urbanization can significantly enhance the likelihood of heavy rainfall in the PRD region, mainly due to the AH effect. Also shown in Figure 3 is the ratio of probability of hourly rain rate in the PRD urban area in the range of 1 to 110mm/hr. It is clear that the impact of urbanization on heavy rainfall (50-110mm/hr) is stronger than that on light rainfall (1-20mm/hr). It can be inferred that, in the range of 1-100mm/hr, the likelihood of rain over urbanized locations, in comparison to cropland, increases as the rainfall intensity increases, with the ratio between AH0 and NO-URBAN being 1 to 1.5, and that between AH300 and NO-URBAN being 1.25 to

3. Based the Kolmogorov-Smirnov (K-S) tests (see Figure S4), there are only a few locations in which the AH0 hourly rain rate in PRD is significantly different from that for NO-URBAN. On the other hand, PDFs of AH300 and NO-URBAN are distinct from each other (at the 95% confidence level) over most of the urban locations.

Figure 4 shows the mean precipitation difference between various numerical experiments, computed by averaging over entire integration periods for all selected extreme cases. Compared with NO-URBAN (see Figure 4a), accumulated rainfall increases slightly over the city area in the AH0 runs. Daily mean rainfall is enhanced by 4 to 6 mm/d over the northeastern corner of the PRD megacity, but otherwise the difference is small (no more than 4 mm/d) over most other urban locations. Moreover, the intensity of rainfall decreases by about 4-12 mm/day in regions such as the eastern part of the urban PRD area. For the AH300 experiment, the averaged rain rate was increased by about 8 to 12 mm/d over most urban grids compared with NO-URBAN (see Figure 4b), with maximum increase of  $\sim 20$  mm/d in the northwestern part of the domain (near cities of Guangzhou and Foshan). The more intense precipitation over these city areas appears to be related to the strong warming at the same locations (see Figure 2c). In our model environment, stronger surface temperature warming related to urbanization tends to result in more rainfall within the PRD megacity. Indeed the aforementioned precipitation change due to land cover change only (AH0 vs NO-URBAN) is insignificant, while that due to both urban land cover and AH, is found to be statistically significant, passing the 95% significance level (see Figure S5).

The above suggests that urbanization can enhance rainfall intensity due to strong warming over the urban area. To further illustrate such a temperature effect, we have plotted the difference of 2-m temperature vs accumulated rainfall over urban grids between AH0 and NO-URBAN, and also those between AH300 and NO-

URBAN (see Figure S6). For AH0, surface warming and rainfall difference are weakly related, whereas a much stronger positive relationship between the two variables can be found for AH300 experiments. Very similar relationship can also be found between extreme precipitation and surface warming (with extreme rainfall defined as the 95th percentile of hourly rain rate throughout the integration periods of all cases considered). It also appears that, at some grid points, large increase of rainfall tend to be associated with small surface warming (see blue box in Figure S6a); further inspection shows that these grid boxes are located at the boundary of the urban area (see red grids in Figure S6b). It seems plausible that enhanced rainfall in these locations was the result of advection of more intense rainfall from the urbanized region in the domain.

### **3.3 Convective instability and moisture transport**

Physically, building materials such as cement and concrete have lower permeability to water vapor, leading to reduced evapotranspiration and less surface evaporation in the urban area compared to cropland (see Figure S7). To ascertain why the rainfall is still increased in the PRD megacity despite suppressed local evaporation, the atmospheric environment and the propensity of convection are further investigated. Figure 5 gives the convective available potential energy (CAPE) and convective inhibition (CIN) difference for parcels lifted at 1000m between AH0 and NO-URBAN, and also between AH300 and NO-URBAN. For AH0 vs NO-URBAN (see Figure 5a), the change of CAPE is small (no more than 10J/kg) in most locations. However, for the AH300 experiment, there is a strong increase of CAPE over the whole urban area compared to NO-URBAN (see Figure 5b), with difference greater than 70J/kg over the norther part of the megacity. Change of CIN is weak (no more than 1.5J/kg) when comparing AH0 with NO-URBAN (see Figure 5c). For

AH300 minus NO-URBAN, CIN gives a strong decrease of more than 5J/kg over the northeastern part of the urban area (see Figure 5d), while for other urban locations the decrease of CIN is about 3-5J/kg. Stronger CAPE and lower CIN create a more unstable atmosphere and convection can be triggered more easily, both consistent with more intense precipitation over the urban area in AH300, compared with NO-URBAN. It can also be seen that the distribution of both CAPE and CIN difference between AH300 and NO-URBAN correspond well with the distribution of the mean rainfall (see Figure 4b).

The vertical profile of the difference of CAPE and CIN averaged over the urban area was also examined (see Figure S8). Both AH0 and AH300 experiments give lower CAPE than NO-URBAN for parcel starting in low levels (lower than 600m) in the urban area (see Figure S8a). This might be related to reduced water vapor content at these levels (see Figure 6), and the higher lapse rate of the virtual temperature for dry parcels. For the AH300 experiment, it can be inferred that CAPE is larger than NO-URBAN at altitudes higher than 600m. Moreover, there is a decrease of CIN at all levels for either AH0 or AH300 compared with NO-URBAN (see Figure S8b). Therefore, it can be said that convection can be triggered more easily due to the presence of megacity with non-zero AH.

The vertical profile of specific humidity from various experiments, and also their differences were also inspected. Figure 6 shows the southwest to northeast cross-section of the difference of mean vertical wind vector and specific humidity over the PRD region between AH0 and NO-URBAN, and also between AH300 and NO-URBAN. Both AH0 and AH300 still give more water vapor than NO-URBAN at higher altitudes, especially for the AH300 experiment. Specific humidity increases more than 0.3g/kg from 0.6km to 2km in AH300, 0.1g/kg at 4.2km and less than

0.1g/kg at 15km (see Figure 6b). Integrating over all levels in the urban area, there is more water vapor in the AH300 runs compared with NO-URBAN. Note that stronger vertical motion in the urban area was found in AH300, which can be attributed to higher CAPE and lower CIN. The increase of specific humidity in higher altitude for AH0, on the other hand, is not as significant as AH300, with no more than 0.1g/kg from 0.2km to 2.5km. Also, the difference in the vertical velocity vector is noisier than that in AH300 (see Figure 6a).

To understand the increase of rainfall and its relationship with moisture transport, Figure 6 gives the vertically integrated difference of water vapor flux and its divergence between AH0 and NO-URBAN, and also between AH300 and NO-URBAN. Both difference of moisture flux vector and divergence are weak between AH0 and NO-URBAN runs: there are even weak northwesterly anomalies over the ocean, which can be attributed to negative temperature difference above 800m between AH0 and NO-URBAN results. But a southwest to northeast directed vector difference can be found in the AH300 minus NO-URBAN moisture flux, indicating stronger moisture transport from the ocean to the urban area. Moreover, stronger convergence is found almost over the whole urban area for AH300, this is especially in the northwestern and eastern urban locations, where the difference of moisture flux divergence can be more than  $-0.04\text{g/m}^2\text{s}^{-1}$  (see Figure 6d). According to the moisture budget equation:

$$\overline{P} - \overline{E} = -\frac{1}{g} \overline{\nabla \cdot \int_{P_r}^{P_s} q \vec{V} dp}$$

the mean rainfall ( $P$ ) equals the sum of surface evaporation ( $E$ ) and vertically integrated moisture flux convergence. Though there is decrease of surface



evaporation due to the presence of megacity, increased moisture flux convergence still leads to more rain over in the same region. Finally, we have also examined the relationship between the prevailing background wind direction and moisture transport. Figure S9 shows the low-level prevailing background wind direction, together with the vertically integrated moisture flux divergence difference between AH300 and NO-URBAN, for each case over the urban area. Here the 950hPa prevailing background wind directions are classified into four types (3 with northeasterly wind, 6 with easterly wind, 15 with southeasterly wind, and 2 with southerly wind). It can be seen that cases with a southerly wind component tends to be associated with stronger moisture flux convergence than those with northerly winds. The above suggests that the background prevailing wind also plays a role in determining the magnitude of the moisture flux convergence effect induced by urbanization.

#### **4. Discussions and Summary**

By utilizing the WRF-SLUCM, sensitivity of extreme precipitation to the level of urbanization described by land use and AH over PRD megacity region was assessed. Parallel experiments were designed by varying the value of surface AH flux (zero or  $300\text{Wm}^{-2}$  as diurnal maximum) and land use types (urban or cropland). As a result, under a highly urbanized scenario, the PRD mega city cluster had strong UHI effects, leading to a higher surface temperature, higher CAPE and lower CIN, and stronger vertical convection. Furthermore, both the intensity and frequency of extreme rainfall in the urban area for the AH300 experiment were increased significantly. The accumulated rainfall increased by more than 12 mm/day, and the probability for strong precipitation is enhanced by 20% at  $10\text{-}20\text{mm/h}^{-1}$  to almost 250% at  $90\text{-}100\text{mm/h}^{-1}$ , when comparing AH300 with NO-URBAN. The above fits well with observations indicating that both the intensity and frequency of extreme rainfall have

increased in the PRD mega city cluster area in recent years (Wang et al. 2016; Wu et al. 2018); here our results suggest that changes in these extreme rainfall characteristics can be rather sensitive to AH released in this region. Enhanced amount of precipitation was also found to be positively related to surface warming. Moreover, the ocean also plays a role in the increased precipitation. Though surface water vapor content was reduced over the urban area due to less surface evaporation, there was more water vapor supply from the South China Sea due to circulation induced by the strong UHI effect in AH300, compared to NO-URBAN, supporting even stronger extreme rainfall over the PRD megacity. On the other hand, though AH0 still have higher urban surface temperature than NO-URBAN, the change of both rainfall intensity and frequency were insignificant; changes in moisture transport and vertical convection in AH0 vs NO-URBAN were also weak. Overall, the comparison between AH300 and NO-URBAN experiment is consistent with results of Fung et al. (2020), who also utilized the WRF-SLUCM for dynamical downscaling and found that high AH can lead to stronger extreme rainfall.

Due to the limitation of SLUCM and lack of land use data when conducting these experiments, only one type of urban land cover was imposed, which gave urban land surface properties that was too homogeneous. With more refined urban use information, more heterogeneous distribution of urban parameter should be incorporated. In the future, we plan to adopt the WRF model coupled with a multiple-layer UCM, with more precise urban parameters in order to better capture the urban physics over the PRD region. We will also focus on urban effect on extreme rainfall under different weather system such as pre-monsoon period and rainfall induced by tropical cyclone.

**Acknowledgments.** This work is jointly supported by the National Key Research and Development Program of China (Ref. No. 2019YFC1510400), the Hong Kong Research Grant Council's General Research Fund (Ref. No. 14308017), and the Pearl River S&T Nova Program of Guangzhou (Ref. No. 201906010054). High performance computation was supported by Information Technology Services Centre of the Chinese University of Hong Kong. All raw data utilized in this study is publicly accessible in the following ways. The GFDL-ESM2M data were from this website- <ftp://nomads.gfdl.noaa.gov/CMIP5/output1/NOAA-GFDL/GFDL-ESM2M/>. The Weather research and forecasting (WRF) model V3.8.1 coupled with single layer urban canopy model (SLUCM) was downloaded online ([https://www2.mmm.ucar.edu/wrf/users/download/get\\_sources.html](https://www2.mmm.ucar.edu/wrf/users/download/get_sources.html)). ERA-Interim was from <https://www.ecmwf.int/en/forecasts/datasets/>. TRMM-3B42 rainfall estimate products are from <https://doi.org/10.5067/TRMM/TMPA/3H/7>. Variables from WRF model output are available on Zenodo (<http://doi.org/10.5281/zenodo.4274053>).

## References

- Adachi, S., Kimura, F., Kusaka, H., Inoue, T., and Ueda, H. (2012). Comparison of the impact of global climate changes and urbanization on summertime future climate in the Tokyo metropolitan area. *Journal of Applied Meteorology and Climatology*, 51(8), 1441-1454. <https://doi.org/10.1175/JAMC-D-11-0137.1>
- Allen, L., Lindberg, F., and Grimmond, C. (2011). Global to city scale urban anthropogenic heat flux: Model and variability. *International Journal of Climatology*, 31(13), 1990-2005. <https://doi.org/10.1002/joc.2210>
- Atkinson, B. (1971). The Effect of an Urban Area on the Precipitation from a Moving Thunderstorm. *Journal of Applied Meteorology* (1962-1982), 10(1), 47-55. [https://doi.org/10.1175/1520-0450\(1971\)010%3C0047:TEOAUA%3E2.0.CO;2](https://doi.org/10.1175/1520-0450(1971)010%3C0047:TEOAUA%3E2.0.CO;2)
- Bae, S., Hong, S., and Lim, K. (2016). Coupling WRF Double-Moment 6-Class Microphysics Schemes to RRTMG Radiation Scheme in Weather Research Forecasting Model. *Advances in Meteorology*, 2016, 1-11. <https://doi.org/10.1155/2016/5070154>
- Bornstein, R., and Lin, Q. (2000). Urban heat islands and summertime convective thunderstorms in Atlanta: three case studies, *Atmospheric Environment*, 34:507–516. [https://doi.org/10.1016/S1352-2310\(99\)00374-X](https://doi.org/10.1016/S1352-2310(99)00374-X)
- Bougeault, P., and P. Lacarrère. (1989). Parameterization of orography-induced turbulence in a mesobeta--scale model. *Monthly Weather Review*, 117(8), 1872-1890. [https://doi.org/10.1175/1520-0493\(1989\)117%3C1872:POOITI%3E2.0.CO;2](https://doi.org/10.1175/1520-0493(1989)117%3C1872:POOITI%3E2.0.CO;2)
- Cao, Q., Yu, D., Georgescu, M., and Wu, J. (2016). Impacts of urbanization on summer climate in China: An assessment with coupled land - atmospheric modeling. *Journal of Geophysical Research: Atmospheres*, 121(18), 10,505-10,521. <https://doi.org/10.1002/2016JD025210>
- Changnon, S. (1968). The La Porte weather anomaly—fact or fiction? *Bulletin of the American Meteorological Society*, 49(1), 4-11. <https://doi.org/10.1175/1520-0477-49.1.4>

- Changnon, S. (1979), Rainfall changes in summer caused by St. Louis, *Science*, 205, 402–404. <https://doi.org/10.1126/science.205.4404.402>
- Changnon, S. (1980). More on the La Porte Anomaly: A Review. *Bulletin of the American Meteorological Society*, 61(7), 702-711. [https://doi.org/10.1175/1520-0477\(1980\)061%3C0702:MOTLPA%3E2.0.CO;2](https://doi.org/10.1175/1520-0477(1980)061%3C0702:MOTLPA%3E2.0.CO;2)
- Changnon, S., and Huff, F. (1986). Urban-related nocturnal rainfall anomaly at St. Louis. *Journal of Climate and Applied Meteorology*, Boston, 25(12), 1985-1995. [https://doi.org/10.1175/1520-0450\(1986\)025%3C1985:TURNRA%3E2.0.CO;2](https://doi.org/10.1175/1520-0450(1986)025%3C1985:TURNRA%3E2.0.CO;2)
- Chen, F., and Dudhia, J. (2001). Coupling and advanced land surface-hydrology model with the Penn State-NCAR MM5 modeling system. Part I: Model implementation and sensitivity. *Monthly Weather Review*, 129(4), 569-585. [https://doi.org/10.1175/1520-0493\(2001\)129%3C0569:CAALSH%3E2.0.CO;2](https://doi.org/10.1175/1520-0493(2001)129%3C0569:CAALSH%3E2.0.CO;2)
- Chen, F., Mitchell, K., Schaake, J., Xue, Y., Pan, H., Koren, V., Duan, Q., Ek, M., and Betts, A. (1996). Modeling of land surface evaporation by four schemes and comparison with fife observations. *Journal of Geophysical Research: Atmospheres*, 101(D3):7251–7268. <https://doi.org/10.1029/95JD02165>
- Chen, F., Kusaka, H., Bornstein, R., Ching, J., Grimmond, C., Grossman-Clarke, S., et al. (2011). The integrated WRF/urban modelling system: Development, evaluation, and applications to urban environmental problems. *International Journal of Climatology*, 31(2), 273-288. <https://doi.org/10.1002/joc.2158>
- Chen, S., Li, W., Du, Y., Mao, C., and Zhang, L. (2015). Urbanization effect on precipitation over the Pearl River Delta based on CMORPH data. *Advances in Climate Change Research*, 6(1), 16-22. <https://doi.org/10.1016/j.accre.2015.08.002>
- Cui, L., and Shi, J. (2012). Urbanization and its environmental effects in Shanghai, China. *Urban Climate*, 2, 1-15. <https://doi.org/10.1016/j.uclim.2012.10.008>

- Dou, J., Wang, Y., Bornstein, R., and Miao, S. (2015). Observed Spatial Characteristics of Beijing Urban Climate Impacts on Summer Thunderstorms. *Journal of Applied Meteorology and Climatology*, 54(1), 94-105. <https://doi.org/10.1175/JAMC-D-13-0355.1>
- Dudhia, J. (1989). Numerical study of convection observed during the Winter Monsoon Experiment using a mesoscale two-dimensional model. *Journal of the Atmospheric Sciences* 46: 3077-3107. [https://doi.org/10.1175/1520-0469\(1989\)046%3C3077:NSOCOD%3E2.0.CO;2](https://doi.org/10.1175/1520-0469(1989)046%3C3077:NSOCOD%3E2.0.CO;2)
- Dunne, J., John, J., Adcroft, A., Griffies, S., Hallberg, R., Shevliakova, E., et al. (2012). GFDL's ESM2 Global Coupled Climate–Carbon Earth System Models. Part I Physical Formulation and Baseline Simulation Characteristics. *Journal of Climate*, 25(19), 6646-6665. <https://doi.org/10.1175/JCLI-D-11-00560.1>
- Dunne, J. (2013). GFDL's ESM2 Global Coupled Climate-Carbon Earth System Models. Part II: Carbon System Formulation and Baseline Simulation Characteristics. *Journal of Climate*, 26(7), 2247-2267. <http://dx.doi.org/10.1175/JCLI-D-12-00150.1>
- Fung, K.W., Tam, C.-Y., Lee, T.C., and Wang, Z. (2020). Comparing the Anthropogenic Heat and Global Warming Impacts on Extreme Precipitation in urbanized Pearl River Delta area based on Dynamical Downscaling. *Geophysical Research Letters*, submitted.
- Gu, Y., and Li, D. (2018). A Modeling Study of the Sensitivity of Urban Heat Islands to Precipitation at Climate Scales. *Urban Climate* 24 2018: 982-93. <https://doi.org/10.1016/j.uclim.2017.12.001>
- Han, J., Baik, J., and Lee, H. (2014). Urban impacts on precipitation. *Asia-Pacific Journal of Atmospheric Sciences*, 50(1), 17-30. <https://doi.org/10.1007/s13143-014-0016-7>
- Han, J., and Pan, H. (2011). Revision of convection and vertical diffusion schemes in the NCEP Global Forecast System. *Weather and Forecasting*, 26(4), 520-533. <https://doi.org/10.1175/WAF-D-10-05038.1>

- Hannah R. (2018). Urbanization. Published online at OurWorldInData.org. Retrieved from “<https://ourworldindata.org/urbanization>”.
- Harnack, R., and Landsberg, H. (1975). Selected Cases of Convective Precipitation Caused by the Metropolitan Area of Washington, D. C. *Journal of Applied Meteorology* (1962-1982), 14(6), 1050-1060. [https://doi.org/10.1175/1520-0450\(1975\)014%3C1050:SCOCPC%3E2.0.CO;2](https://doi.org/10.1175/1520-0450(1975)014%3C1050:SCOCPC%3E2.0.CO;2)
- Holst, C., Tam, C., and Chan, J. (2016). Sensitivity of urban rainfall to anthropogenic heat flux: A numerical experiment. *Geophysical Research Letters*, 43(5), 2240-2248. <https://doi.org/10.1002/2015GL067628>
- Holst, C. C., Chan, J., and C.-Y. Tam, (2017). Sensitivity of Precipitation Statistics to Urban Growth in a Subtropical Coastal Megacity Cluster. *Journal of Environmental. Sciences*, 59, 6-12. <https://doi.org/10.1016/j.jes.2017.01.004>
- Hong, S., Noh, Y., and Dudhia, J. (2006). A New Vertical Diffusion Package with an Explicit Treatment of Entrainment Processes. *Monthly Weather Review*, 134(9), 2318-2341. <https://doi.org/10.1175/MWR3199.1>
- Hou, A., Ni, G., Yang, H., and Lei, Z. (2013). Numerical Analysis on the Contribution of Urbanization to Wind Stilling an Example over the Greater Beijing Metropolitan Area. *Journal of Applied Meteorology and Climatology*, 52(5), 1105-1115. <https://doi.org/10.1175/JAMC-D-12-013.1>
- Huang, D., and Gao, S. (2018). Impact of different reanalysis data on WRF dynamical downscaling over China. *Atmospheric Research*, 200, 25-35. <https://doi.org/10.1016/j.atmosres.2017.09.017>
- Huang, H., Ooka, R., and Kato, S. (2005). Urban thermal environment measurements and numerical simulation for an actual complex urban area covering a large district heating and cooling system in summer. *Atmospheric Environment*, 39(34), 6362-6375. <https://doi.org/10.1016/j.atmosenv.2005.07.018>
- Huff, F., and Changnon, S. (1972). Climatological Assessment of Urban Effects on Precipitation at St. Louis. *Journal of Applied Meteorology* (1962-1982), 11(5),

823-842. [https://doi.org/10.1175/1520-0450\(1972\)011%3C0823:CAOUEO%3E2.0.CO;2](https://doi.org/10.1175/1520-0450(1972)011%3C0823:CAOUEO%3E2.0.CO;2)

- Hutcheon, R., Johnson, R., Lowry, W., Black, C., and Hadley, D. (1967). Observations of the urban heat island in a small city. *Bulletin of the American Meteorological Society*, 48(1), 7-9. <http://www.jstor.org/stable/26248882>
- Iacono, M., Delamere, J., Mlawer, E., Shephard, M., Clough, S., and Collins, W. (2008), Radiative forcing by long-lived greenhouse gases: Calculations with the AER radiative transfer models. *Journal of Geophysical Research*., 113(D13103). <https://doi.org/10.1029/2008JD009944>
- Iwashima, T., and Yamamoto, R. (1993). A statistical analysis of the extreme events: Long-term trend of heavy daily precipitation. *Journal of the Meteorological Society of Japan*, 71(5), 637-640. [https://doi.org/10.2151/jmsj1965.71.5\\_637](https://doi.org/10.2151/jmsj1965.71.5_637)
- Janjic, Z. (1994). The step-mountain Eta coordinate model: Further developments of the convection, viscous sublayer, and turbulence closure schemes. *Monthly Weather Review*, 122: 927-945. [https://doi.org/10.1175/1520-0493\(1994\)122%3C0927:TSMECM%3E2.0.CO;2](https://doi.org/10.1175/1520-0493(1994)122%3C0927:TSMECM%3E2.0.CO;2)
- Jin, M., Li, Y., and Su, D. (2015). Urban-Induced Mechanisms for an Extreme Rainfall Event in Beijing China: A Satellite Perspective. *Climate*, 3(1), 193–209. <https://doi.org/10.3390/cli3010193>
- Krishtawal, C., Niyogi, D., Tewari, M., Pielke, R., and Shepherd, M. (2010), Urbanization signature in the observed heavy rainfall climatology over India. *International Journal of Climatology*, 30(13), 1908-1916. <https://doi.org/10.1002/joc.2044>
- Kusaka, H., Kondo, H., Kikegawa, Y., and Kimura, F. (2001). A Simple Single-Layer Urban Canopy Model for Atmospheric Models: Comparison with Multi-Layer and Slab Models. *Boundary-Layer Meteorology*, 101(3), 329-358. <https://doi.org/10.1023/A:1019207923078>
- Kusaka, H., Nawata, K., Suzuki-Parker, A., Takane, Y., and Furuhashi, N. (2014). Mechanism of Precipitation Increase with Urbanization in Tokyo as Revealed



- by Ensemble Climate Simulations. *Journal of Applied Meteorology and Climatology*, 53(4), 824-839. <https://doi.org/10.1175/JAMC-D-13-065.1>
- Langenberg, H, and Feser, F. (2000). A Spectral Nudging Technique for Dynamical Downscaling Purposes. *Monthly Weather Review*, 128(10), 3664–3673. [https://doi.org/10.1175/1520-0493\(2000\)128%3C3664:ASNTFD%3E2.0.CO;2](https://doi.org/10.1175/1520-0493(2000)128%3C3664:ASNTFD%3E2.0.CO;2)
- Lin, C., Chen, W., Liu, S., Liou, Y., Liu, G., and Lin, T. (2008). Numerical study of the impact of urbanization on the precipitation over Taiwan. *Atmospheric Environment*, 42(13), 2934-2947. <https://doi.org/10.1016/j.atmosenv.2007.12.054>
- Liu, J. and Niyogi, D. (2019). Meta-analysis of urbanization impact on rainfall modification. *Scientific Reports*, 9(1), 7301. <https://doi.org/10.1038/s41598-019-42494-2>
- McSweeney, C. F., Jones, R. G., Lee, R. W., and Rowell, D. P. (2015). Selecting CMIP5 GCMs for downscaling over multiple regions. *Climate Dynamics*, 44(11–12), 3237–3260. <https://doi.org/10.1007/s00382-014-2418-8>
- Miao, S., Chen, F., Li, Q., and Fan, S. (2011). Impacts of urban processes and urbanization on summer precipitation: A case study of heavy rainfall in Beijing on 1 August 2006. *Journal of Applied Meteorology and Climatology*, 50(4), 806-825. <https://doi.org/10.1175/2010JAMC2513.1>
- Miao, S., Li, Q., Wang, Y., Chen, F., LeMone, M., and Tewari, M. (2009). An observational and modeling study of characteristics of urban heat island and boundary layer structures in Beijing. *Journal of Applied Meteorology and Climatology*, 48(3), 484-501. <https://doi.org/10.1175/2008JAMC1909.1>
- Mlawer, E., Taubman, S., Brown, P., Iacono, M., and Clough, S. (1997). Radiative transfer for inhomogeneous atmospheres: RRTM, a validated correlated-k model for the longwave. *Journal of Geophysical Research: Atmospheres*, 102(D14), 16663-16682. <https://doi.org/10.1029/97JD00237>
- Mohajerani, A., Bakaric, J., and Jeffrey-Bailey, T. (2017). The urban heat island effect, its causes, and mitigation, with reference to the thermal properties of

- asphalt concrete. *Journal of Environmental Management*, 197, 522-538.  
<https://doi.org/10.1016/j.jenvman.2017.03.095>
- Oke, T. (1973). City size and the urban heat island. *Atmospheric Environment*, 7(8), 769-779. [https://doi.org/10.1016/0004-6981\(73\)90140-6](https://doi.org/10.1016/0004-6981(73)90140-6)
- Oke, T. (1976). The distinction between canopy and boundary layer urban heat islands. *Atmosphere*, 14(July 2015), 268-277.  
<https://doi.org/10.1080/00046973.1976.9648422>
- Oke, T. (1981). Canyon geometry and the nocturnal urban heat island: comparison of scale model and field observations. *Journal of Climatology*, 1, 237-254.  
<https://doi.org/10.1002/joc.3370010304>
- Oke, T. (1988). The urban energy balance. *Progress in Physical Geography*, 12(491).  
<https://doi.org/10.1177%2F030913338801200401>
- Orville, R., Huffines, G., Nielsen - Gammon, J., Zhang, R., Ely, B., Steiger, S., et al. (2001). Enhancement of cloud - to - ground lightning over Houston, Texas. *Geophysical Research Letters*, 28(13), 2597-2600.  
<https://doi.org/10.1029/2001GL012990>
- Paul, S., Ghosh, S., Mathew, M., Devanand, A., Karmakar, S., and Niyogi, D. (2018). Increased Spatial Variability and Intensification of Extreme Monsoon Rainfall due to Urbanization. *Science Report*, 8(1), 3918.  
<https://doi.org/10.1038/s41598-018-22322-9>
- Shastri, H., Paul, S., Ghosh, S., and Karmakar, S. (2015). Impacts of urbanization on Indian summer monsoon rainfall extremes. *Journal of Geophysical Research: Atmospheres*, 120(2), 496-516. <https://doi.org/10.1002/2014JD022061>
- Shepherd, J. (2006). Evidence of urban-induced precipitation variability in arid climate regimes. *Journal of Arid Environments*, 67(4), 607-628.  
<https://doi.org/10.1016/j.jaridenv.2006.03.022>
- Shepherd, J., and Burian, S. (2003). Detection of Urban-Induced Rainfall Anomalies in a Major Coastal City. *Earth Interactions*, 7, Earth Interactions, 2003, Vol.7.

[https://doi.org/10.1175/1087-3562\(2003\)007%3C0001:DOUIRA%3E2.0.CO;2](https://doi.org/10.1175/1087-3562(2003)007%3C0001:DOUIRA%3E2.0.CO;2)

- Shem, W., and Shepherd, M. (2009). On the impact of urbanization on summertime thunderstorms in Atlanta: Two numerical model case studies. *Atmospheric Research*, 92(2), 172-189. <https://doi.org/10.1016/j.atmosres.2008.09.013>
- Shimadera, H., Kondo, A., Shrestha, K., Kitaoka, K., and Inoue, Y. (2015). Numerical Evaluation of the Impact of Urbanization on Summertime Precipitation in Osaka, Japan. *Advances in Meteorology*, 2015(2015), 149-159. <https://doi.org/10.1155/2015/379361>
- Skamarock, W., Klemp, J., Dudhia, J., Gill, D., Barker, D., Duda, M., Huang, X., Wang, W., and Powers, J. (2008), A description of the advanced research WRF version 3 NCAR Tech. Note, NCAR/TN-475+STR. <http://dx.doi.org/10.5065/D68S4MVH>
- Soltani, A., and Sharifi, E. (2017). Daily variation of urban heat island effect and its correlations to urban greenery: A case study of Adelaide. *Frontiers of Architectural Research*, 6(4), 529-538. <https://doi.org/10.1016/j.foar.2017.08.001>
- Tayanç, M., and Toros, H. (1997). Urbanization effect on regional climate change in the case of four large cities of Turkey. *Climatic Change*, 35(4), 501-524. <https://doi.org/10.1023/A:1005357915441>
- Tewari, M. F., Chen, F., Kusaka, H., and Miao, S. (2008). Coupled WRF/Unified Noah/urban-canopy modeling system, NCAR WRF Documentation, NCAR, Boulder, 1–20.
- Vukovich, F., and King, W. (1980). A Theoretical Study of the St. Louis Heat Island: Comparisons Between Observed Data and Simulation Results on the Urban Heat Island Circulation. *Journal of Applied Meteorology* (1962-1982), 19(7), 761-770. [https://doi.org/10.1175/1520-0450\(1980\)019%3C0761:ATSOTS%3E2.0.CO;2](https://doi.org/10.1175/1520-0450(1980)019%3C0761:ATSOTS%3E2.0.CO;2)

- Wang, D., Jiang, P., Wang, G., and Wang, D. (2015). Urban extent enhances extreme precipitation over the Pearl River Delta, China. *Atmospheric Science Letters*, 16(3), 310-317. <https://doi.org/10.1002/asl2.559>
- Wang, J., Feng, J., and Yan, Z. (2015). Potential sensitivity of warm season precipitation to urbanization extents: Modeling study in Beijing - Tianjin - Hebei urban agglomeration in China. *Journal of Geophysical Research: Atmospheres*, 120(18), 9408-9425. <https://doi.org/10.1002/2015JD023572>
- Wong, M., Yang, J., Weng, Q., Menenti, M., and Chan, P. (2015). Modeling of Anthropogenic Heat Flux Using HJ-1B Chinese Small Satellite Image: A Study of Heterogeneous Urbanized Areas in Hong Kong. *IEEE Geoscience and Remote Sensing Letters*, 12(7), 1466-1470. <https://doi.org/10.1109/LGRS.2015.2409111>
- Wu, L., and Zhang, J. (2018). Assessing population movement impacts on urban heat island of Beijing during the Chinese New Year holiday: Effects of meteorological conditions. *Theoretical and Applied Climatology*, 131(3), 1203-1210. <https://doi.org/10.1007/s00704-017-2043-7>
- Xiao, Z., Wang, Z., Huang, M., Luo, X., Liang, Y., and Lin, Z. (2020). Urbanization in an underdeveloped city-Nanning, China and its impact on a heavy rainfall event in July. *Earth and Space Science*, 7, e2019EA000991. <https://doi.org/10.1029/2019EA000991>
- Yan, M., Chan, J., and Zhao, K. (2020). Impacts of Urbanization on the Precipitation Characteristics in Guangdong Province, China. *Advances in Atmospheric Sciences*, 37(7), 696-706. <https://doi.org/10.1007/s00376-020-9218-3>
- Yang, L., Scheffran, J., Qin, H., and You, Q. (2015). Climate-related flood risks and urban responses in the Pearl River Delta, China. *Regional Environmental Change*, 15(2), 379-391. <https://doi.org/10.1007/s10113-014-0651-7>
- Zhang, Y., Miao, S., Dai, Y., and Bornstein, R. (2017). Numerical simulation of urban land surface effects on summer convective rainfall under different UHI

intensity in Beijing. Journal of Geophysical Research: Atmospheres, 122(15), 7851-7868. <https://doi.org/10.1002/2017JD026614>

<b>UCM parameter</b>	<b>High intensity residence</b>
<b>Anthropogenic heat (diurnal maximum) [W m<sup>-2</sup>]</b>	<b>300.0</b>
<b>Building height [m]</b>	<b>30</b>
<b>Urban fraction</b>	<b>0.9</b>
<b>Standard Deviation of roof height [m]</b>	<b>4.0</b>
<b>Roof width [m]</b>	<b>9.4</b>
<b>Road width [m]</b>	<b>16.0</b>
<b>Surface albedo of road</b>	<b>0.2</b>
<b>Surface albedo of roof</b>	<b>0.2</b>
<b>Surface albedo of building wall</b>	<b>0.2</b>

**Table 1** Values of UCM parameters prescribed for the urban land use category.

### **Figure captions**

**Figure 1** (a) Nested domains for the WRF simulations. (b) Land use categories in innermost domain for AH0 and AH300 experiments, based on 2002 MODIS data with urban and build-up, cropland, forest and grassland shown areas in red, yellow, cyan and green. Also shown are locations of major cities in PRD (denoted by black dots, counterclockwise from lower right): Hong Kong (HK), Shenzhen (SZ), Dongguan (DG), Guangzhou (GZ), Foshan (FS), Zhongshan (ZS), Zhuhai (ZH) and Macao (MC). See text for details. (c) Land use categories for the NOURBAN experiment, in which urban and build-up areas are replaced by cropland.

**Figure 2** Surface albedo difference between (a) AH0 and NO-URBAN, and 2-m temperature difference (units: °C) between (b) AH0 and NO-URBAN and (c) AH300 and NO-URBAN. Temperature values are computed by averaging over entire integrations for all selected extreme cases. See text for details. The urban area within PRD is outlined by black contours.

**Figure 3** (a) PDFs of hourly precipitation rates over urban locations within PRD, within the ranges of 1-10, 10-20, 20-30, 30-40, 40-50, 50-60, 60-70, 70-80, 80-90, 90-100, and 100-110 mm/hr (denoted by 10, 20, 30, 40, 50, 60, 70, 80, 90, 100, 110mm/h, respectively) for the NO-URBAN (black), AH0 (blue), AH300 (red) experiments. (b) Ratio of the probabilities between AH0 and NO-URBAN (blue), and that between AH300 and NO-URBAN (blue) at different precipitation rates.

**Figure 4** Precipitation rate (units: mm/d) difference between (a) AH0 and NO-URBAN and (c) AH300 and NO-URBAN, averaged over entire integrations for all selected extreme cases.

**Figure 5** Same as Figure 4 except for (a,b) CAPE (units: J/kg) and (c,d) CIN (units: J/kg). CAPE and CIN values are computed by averaging over entire integrations for all selected extreme cases, and for parcels rising at 1000m of height.

**Figure 6** Difference in (a,b) wind (vector; see scale arrow at lower left) and specific humidity (shading) on a cross-sectional plan (southwest to northeast), and (c,d) vertically integrated moisture flux (vector: see scale arrow at lower left) and its divergence (shading) between (a,c) AH0 and NO-URBAN; (b,d) AH300 and NO-URBAN. Values are calculated by summing over entire integrations for selected extreme cases. See text for details. The urban area within PRD is outlined in (c,d) by black contours; direction of cross section in (a,c) is shown by green lines in (c,d).

**Figure S1** Same as Figure 1a except for ratio of surface albedo.

**Figure S2** Vertical profile of temperature difference, averaged over urban grids in the innermost domain, between AH0 and NO-URBAN (blue), and between AH300 and NO-URBAN (red). Temperatures values are computed by averaging over entire integrations for all selected extreme cases.

**Figure S3** Same as Figure 4 except for cloud fraction averaged over all layers (units: %).

**Figure S4** Same as Figure S6 except for results of the K-S test for the difference of PDFs of hourly precipitation rates.

**Figure S5** Results of Student's t-test for daily mean rainfall difference between (a) AH0 and NO-URBAN, (b) AH300 and NO-URBAN. Locations in which the difference exceeds the 95% significance levels are denoted by black dots. The urban area within PRD is outlined by black contours.

**Figure S6** (a) Scatter plot of temperature difference vs daily rainfall difference between AH0 and NO-URBAN (blue), and between AH300 and NO-URBAN (red) over all urban grid boxes. (b) Location of grids for temperature difference less than 2°C and rainfall difference larger than 5mm/day between AH300 and NO-URBAN (data in blue rectangle of Figure S5a). (c) Same as Figure S5a except for extreme rainrate difference. Extreme rainrate is defined as rainrate larger than 95th percentile of hourly rainfall, based on all selected rainfall events.

**Figure S7** Same as Figure 4 except for surface evaporation (units:  $\text{g}\cdot\text{m}^{-2}\cdot\text{s}^{-2}$ ).

**Figure S8** (a) CAPE and (b) CIN, as functions of height at which parcels begin to rise, from NO-URBAN (black), AH0 (blue) and AH300 (red). CAPE and CIN are computed by averaging values over urban grids in the innermost domain, over entire integrations for all selected extreme cases.

**Figure S9** Moisture flux divergence for each case of AH300, the value was calculated by summing over entire integrations for all urban grids in selected extreme cases. Abscissa represents the low-level prevailing wind direction in urban area for each case: northeast (black), east (blue), southeast (red), and southwest (yellow). See text for details.

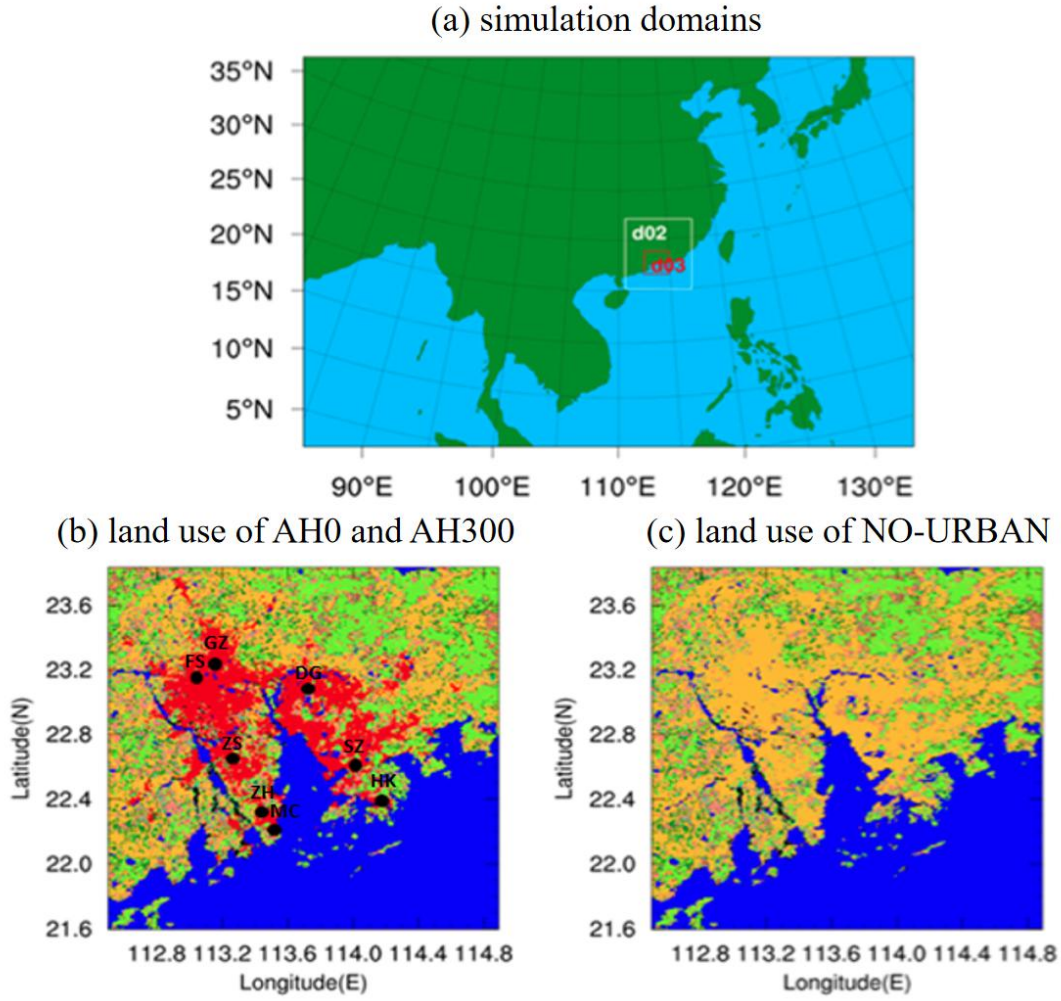


**Figure 1** (a) Nested domains for the WRF simulations. (b) Land use categories in innermost domain for AH0 and AH300 experiments, based on 2002 MODIS data with urban and build-up, cropland, forest and grassland shown areas in red, yellow, cyan and green. Also shown are locations of major cities in PRD (denoted by black dots, counterclockwise from lower right): Hong Kong (HK), Shenzhen (SZ), Dongguan (DG), Guangzhou (GZ), Foshan (FS), Zhongshan (ZS), Zhuhai (ZH) and Macao (MC). See text for details. (c) Land use categories for the NOURBAN experiment, in which urban and build-up areas are replaced by cropland.



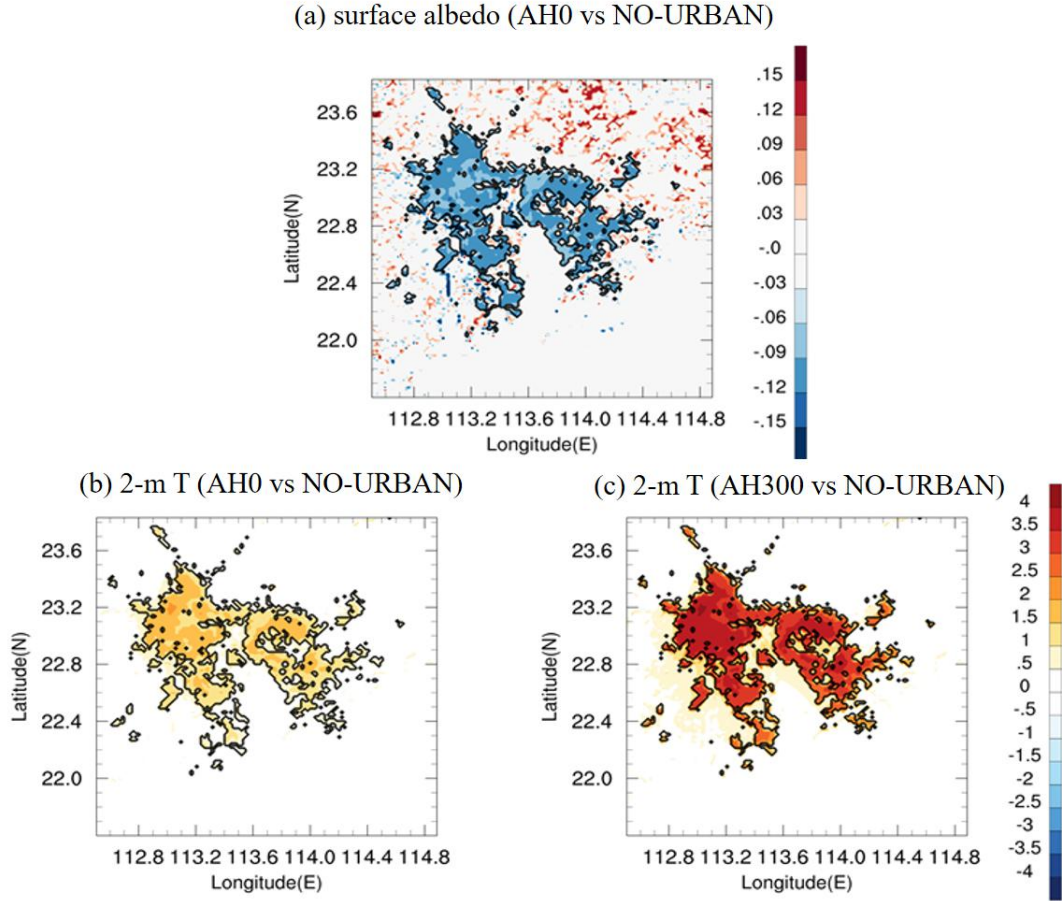


**Figure 2** Surface albedo difference between (a) AH0 and NO-URBAN, and 2-m temperature difference (units: °C) between (b) AH0 and NO-URBAN and (c) AH300 and NO-URBAN. Temperature values are computed by averaging over entire integrations for all selected extreme cases. See text for details. The urban area within PRD is outlined by black contours.

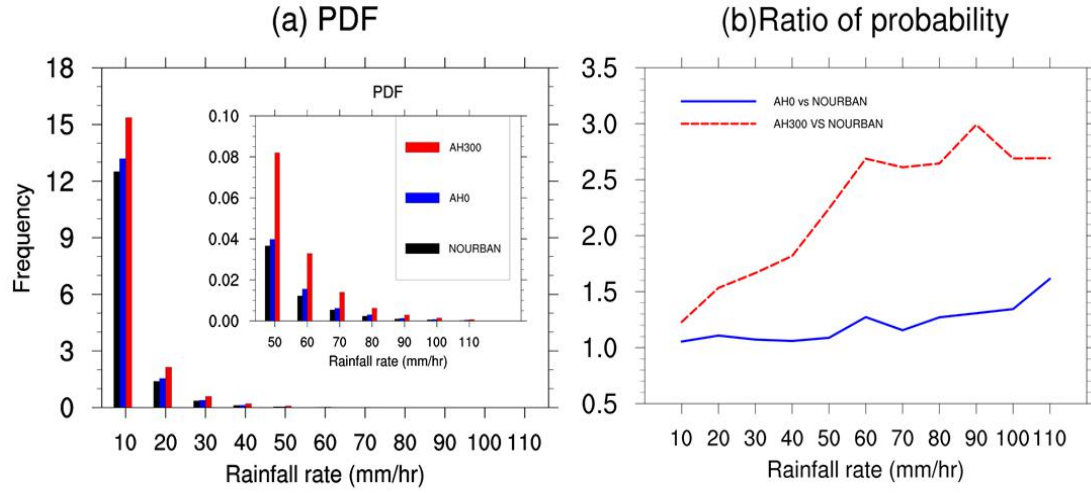


**Figure 3** (a) PDFs of hourly precipitation rates over urban locations within PRD, within the ranges of 1-10, 10-20, 20-30, 30-40, 40-50, 50-60, 60-70, 70-80, 80-90, 90-100, and 100-110 mm/hr (denoted by 10, 20, 30, 40, 50, 60, 70, 80, 90, 100, 110mm/h, respectively) for the NO-URBAN (black), AH0 (blue), AH300 (red) experiments. (b) Ratio of the probabilities between AH0 and NO-URBAN (blue), and that between AH300 and NO-URBAN (blue) at different precipitation rates.

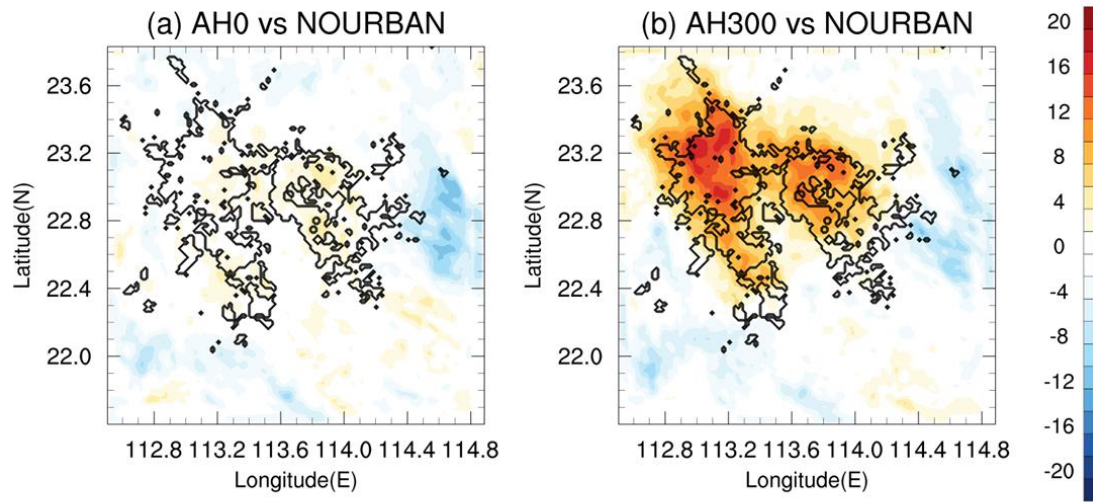


**Figure 4** Precipitation rate (units: mm/d) difference between (a) AH0 and NO-URBAN and (c) AH300 and NO-URBAN, averaged over entire integrations for all selected extreme cases.

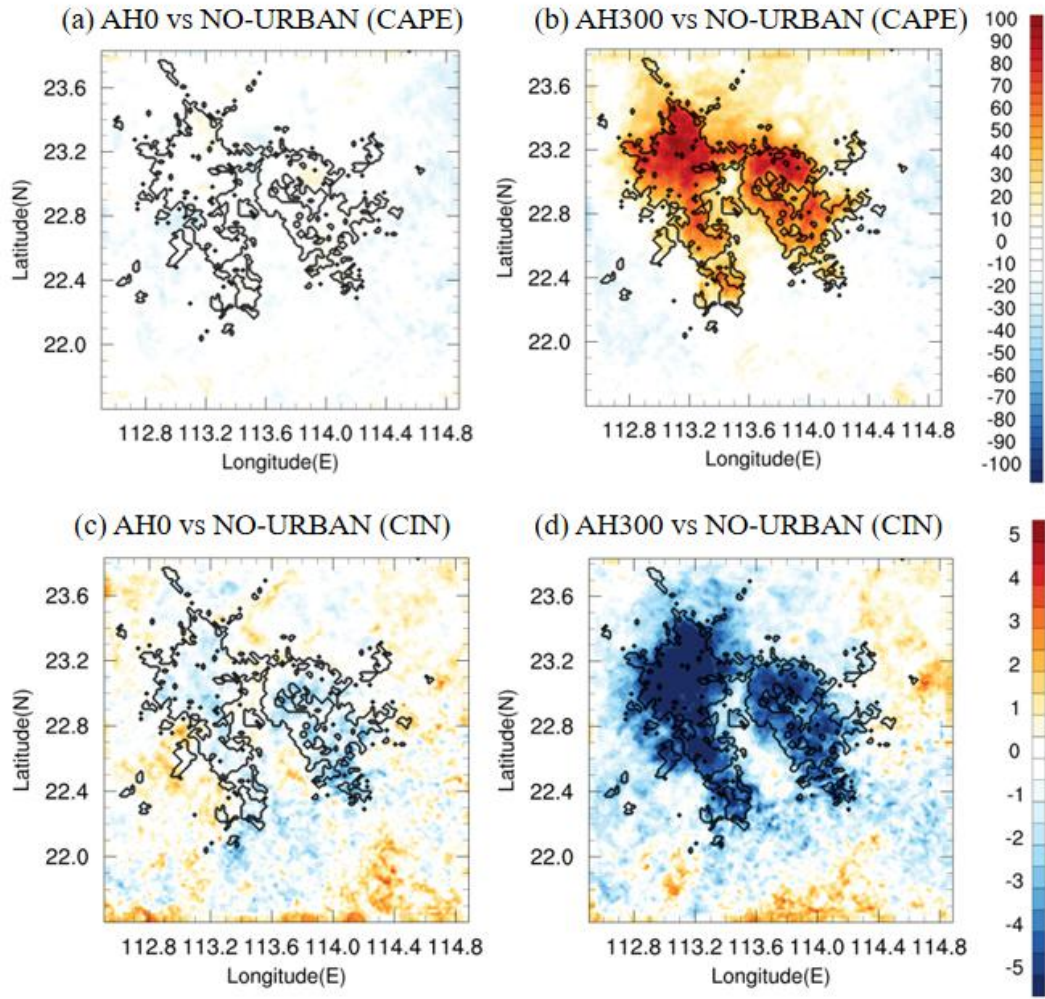


**Figure 5** Same as Figure 4 except for (a,b) CAPE (units: J/kg) and (c,d) CIN (units: J/kg). CAPE and CIN values are computed by averaging over entire integrations for all selected extreme cases, and for parcels rising at 1000m of height.

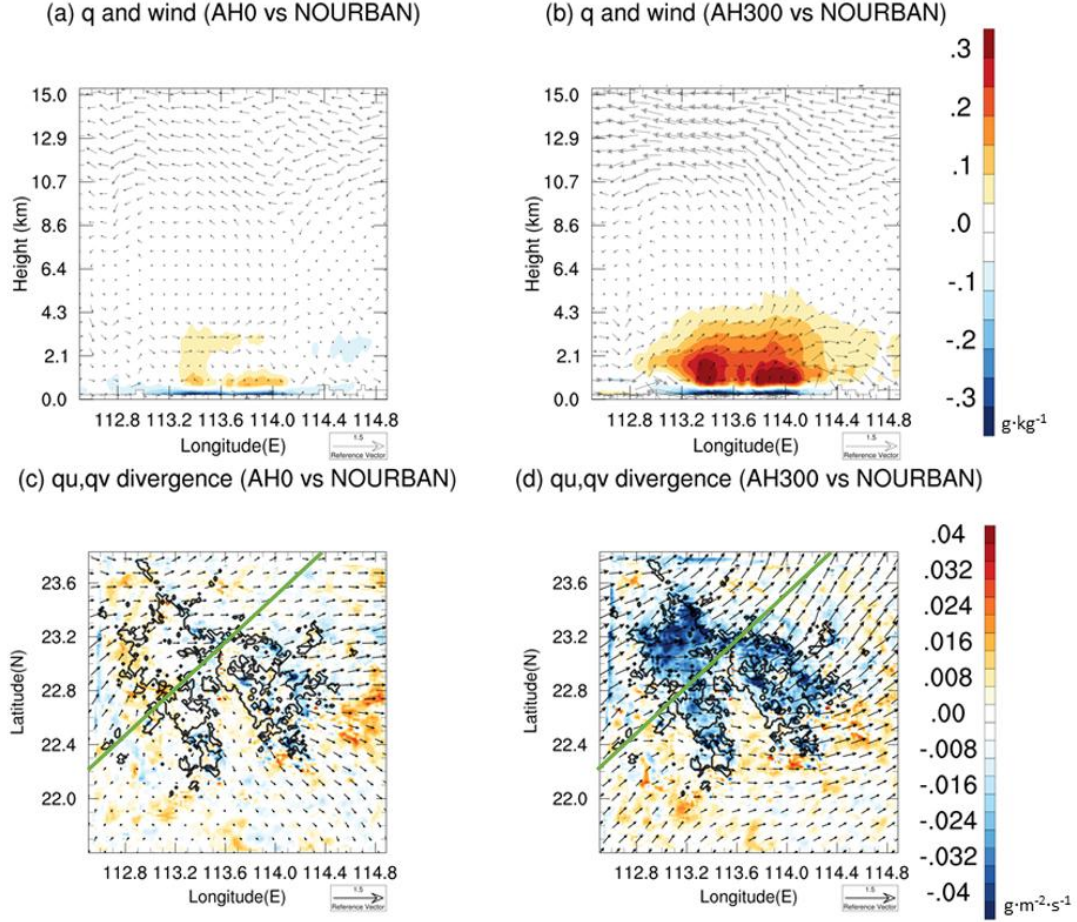


**Figure 6** Difference in (a,b) wind (vector; see scale arrow at lower left) and specific humidity (shading) on a cross-sectional plan (southwest to northeast), and (c,d) vertically integrated moisture flux (vector: see scale arrow at lower left) and its divergence (shading) between (a,c) AH0 and NO-URBAN; (b,d) AH300 and NO-URBAN. Values are calculated by summing over entire integrations for selected extreme cases. See text for details. The urban area within PRD is outlined in (c,d) by black contours; direction of cross section in (a,c) is shown by green lines in (c,d).



## Supplementary figures

Ratio of albedo (AH0 vs NO-URBAN)

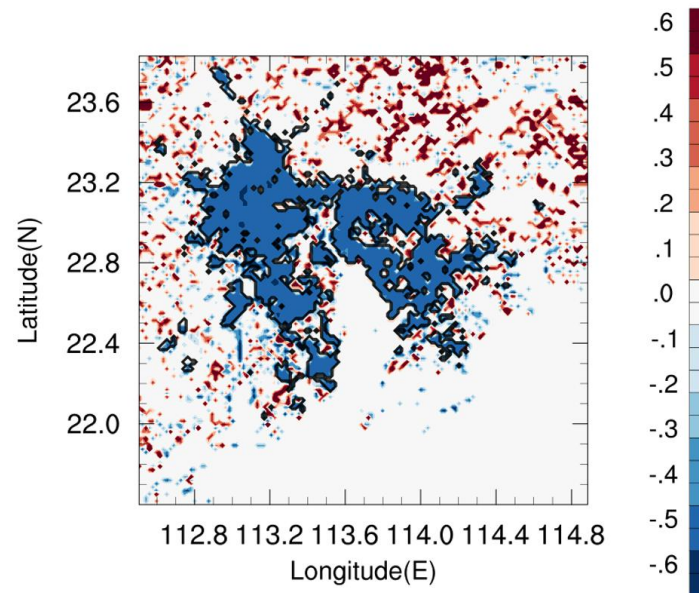


**Figure S1** Same as Figure 1a except for ratio of surface albedo.

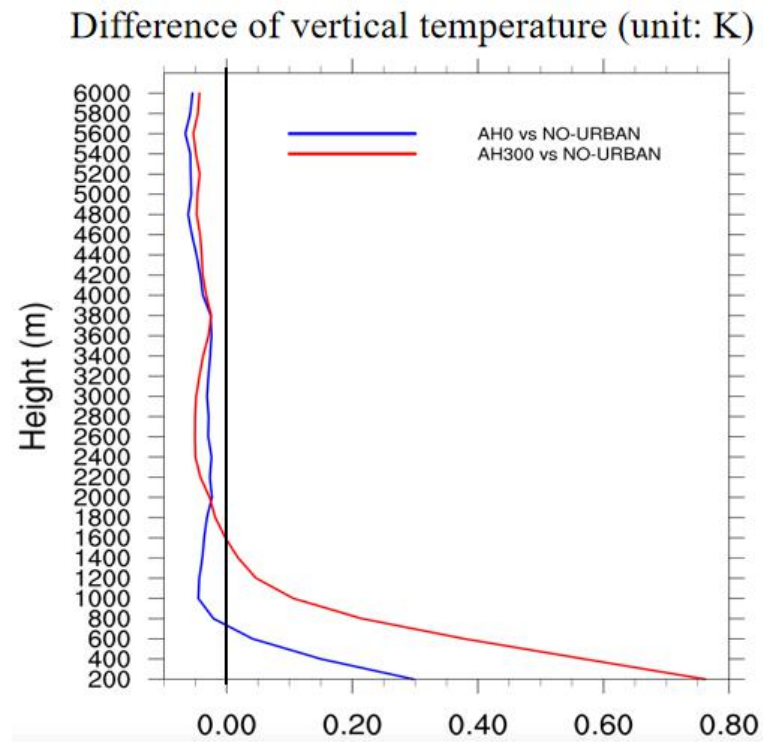


**Figure S2** Vertical profile of temperature difference, averaged over urban grids in the innermost domain, between AH0 and NO-URBAN (blue), and between AH300 and NO-URBAN (red). Temperatures values are computed by averaging over entire integrations for all selected extreme cases.

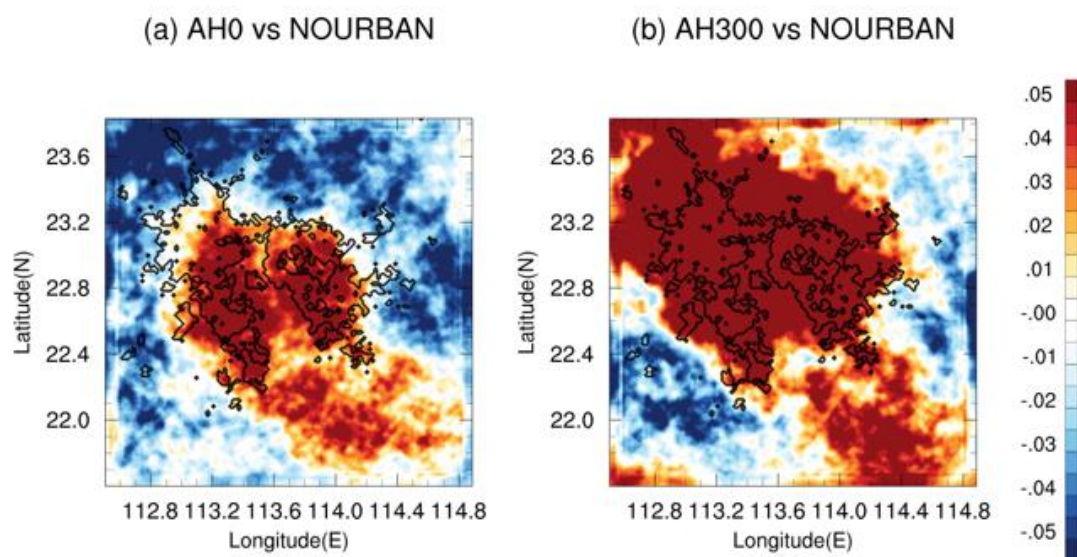


**Figure S3** Same as Figure 4 except for cloud fraction averaged over all layers (units: %).



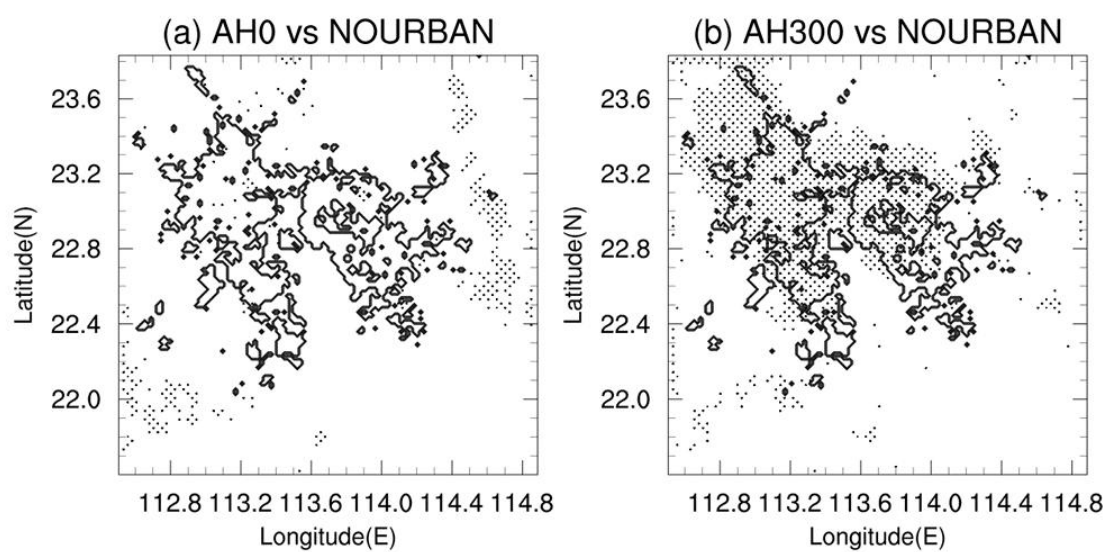


**Figure S4** Same as Figure S6 except for results of K-S test for the difference of PDFs of hourly precipitation rates.

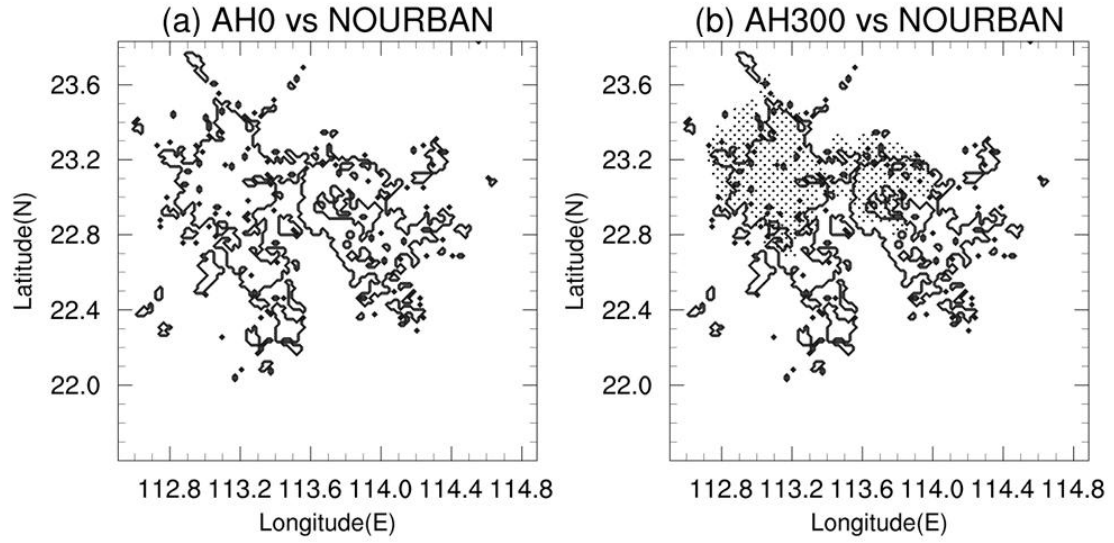


**Figure S5** Results of Student's t-test for daily mean rainfall difference between (a) AH0 and NO-URBAN, (b) AH300 and NO-URBAN. Locations in which the difference exceeds the 95% significance level are denoted by black dots. The urban area within PRD is outlined by black contours.

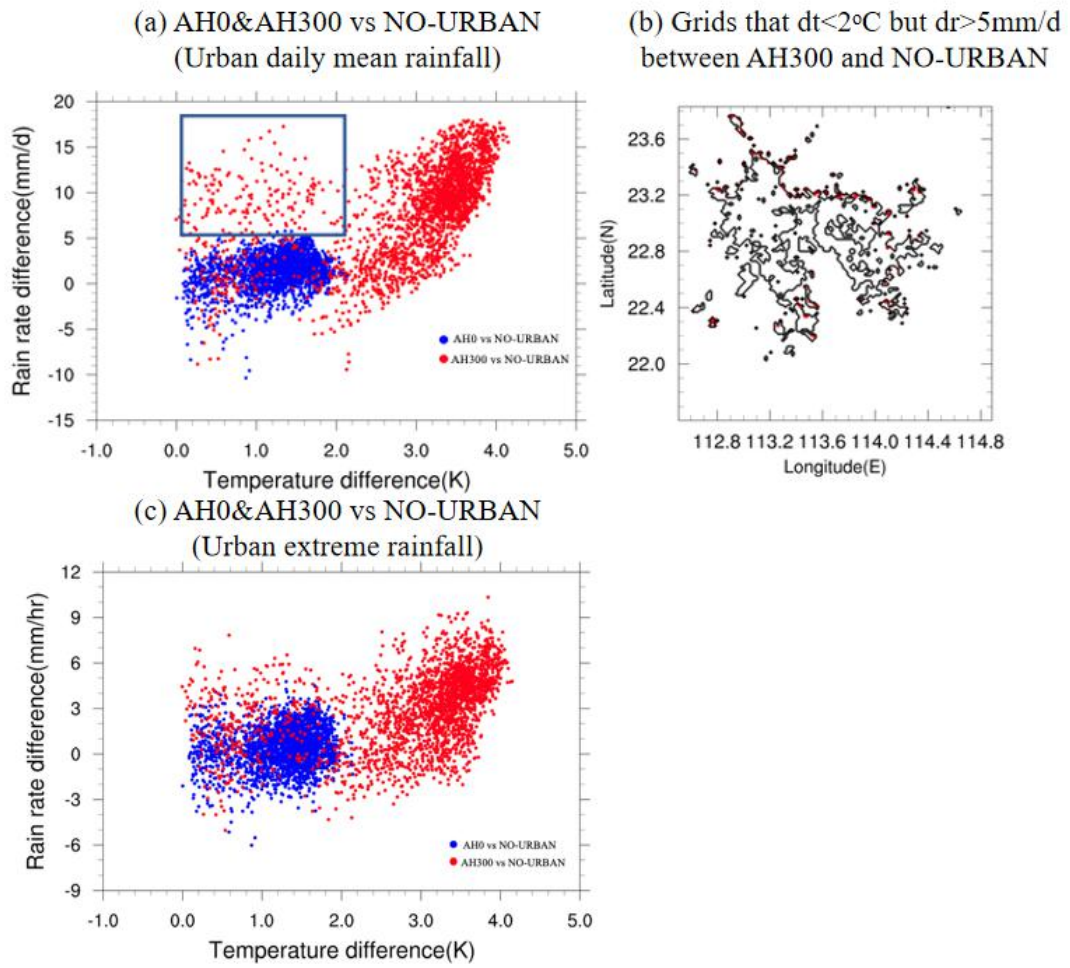


**Figure S6** (a) Scatter plot of temperature difference vs daily rainfall difference between AH0 and NO-URBAN (blue), and between AH300 and NO-URBAN (red) over all urban grid boxes. (b) Location of grids for temperature difference less than  $2^{\circ}\text{C}$  and rainfall difference larger than  $5\text{mm/day}$  between AH300 and NO-URBAN (data in blue rectangle of Figure S5a). (c) Same as Figure S5a except for extreme rain rate difference. Extreme rain rate is defined as rain rate larger than 95th percentile of hourly rainfall, based on all selected rainfall events.

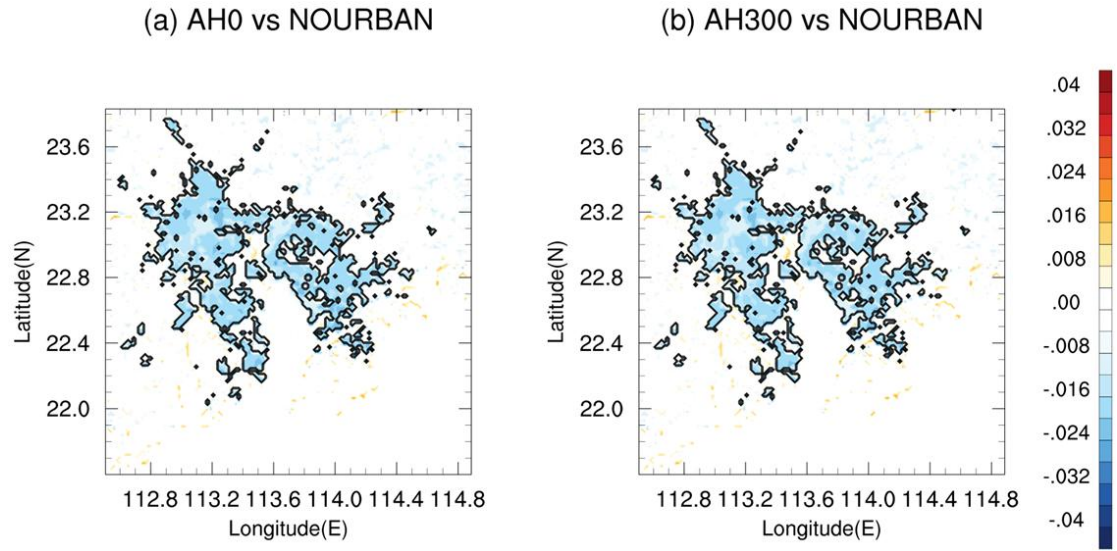


**Figure S7** Same as Figure 4 except for surface evaporation (units:  $\text{g}\cdot\text{m}^{-2}\cdot\text{s}^{-2}$ ).

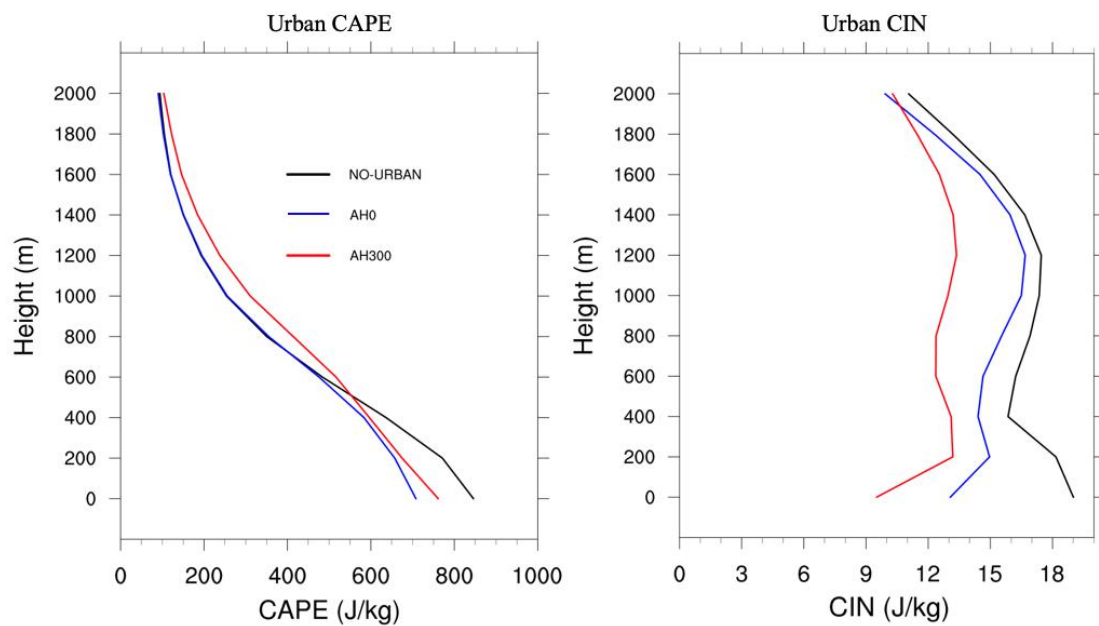


**Figure S8** (a) CAPE and (b) CIN, as functions of height at which parcels being to rise, from NO-URBAN (black), AH0 (blue) and AH300 (red). CAPE and CIN are computed by averaging values over urban grids in the innermost domain, over entire integrations for all selected extreme cases.

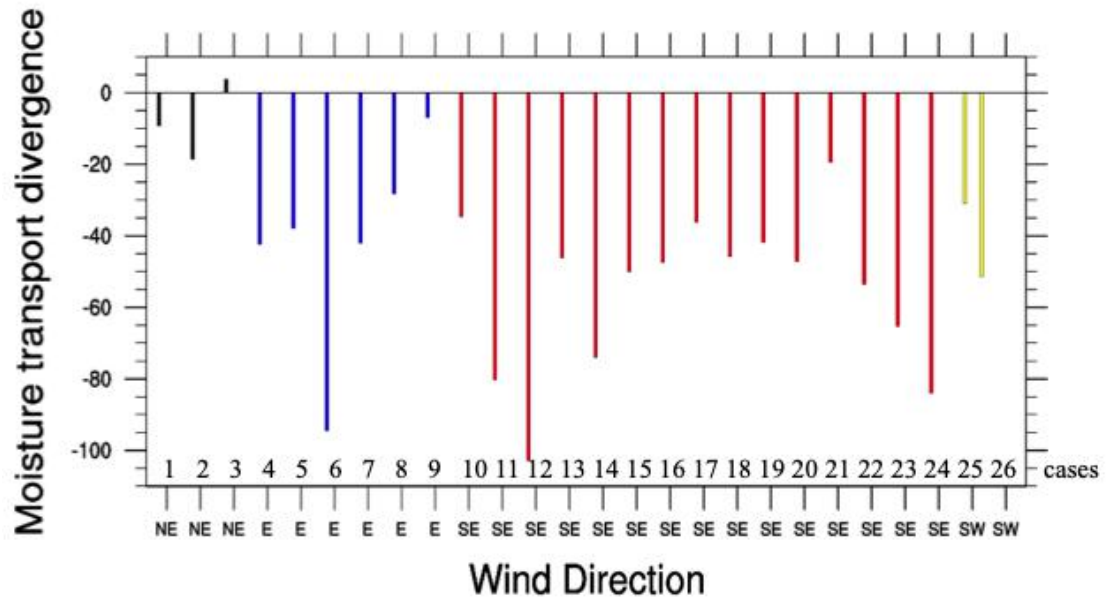


**Figure S9** Moisture flux divergence for each case of AH300, the value was calculated by summing over entire integrations for all urban grids in selected extreme cases. Abscissa represents the low-level prevailing wind direction in urban area for each case: northeast (black), east (blue), southeast (red), and southwest (yellow). See text for details.